A Switchable Longitudinal & Shear BLS Microscope for Comprehensive Modulus Imaging of Semiconductor Packaging Materials

Andrew J. Gayle
[1]*National Institute of Standards and Technology*
Gaithersburg, MD, USA
[2]*University of Maryland*
College Park, MD, USA
ORCID: 0000-0003-4802-2439

Sebastian Engmann
[1]*Theiss Research*
La Jolla, CA, USA
[2]*National Institute of Standards and Technology*
Gaithersburg, MD, USA
ORCID: 0000-0001-8791-3432

Ran Tao
National Institute of Standards and Technology
Gaithersburg, MD, USA
ORCID: 0000-0002-5208-7895

Andrew G. Korovich
National Institute of Standards and Technology
Gaithersburg, MD, USA
ORCID: 0000-0003-3736-1523

Polette Centellas
National Institute of Standards and Technology
Gaithersburg, MD, USA
ORCID: 0000-0003-3248-3409

Yvonne B. Gerbig
National Institute of Standards and Technology
Gaithersburg, MD, USA
ORCID: 0000-0002-8947-4215

Christopher L. Soles
National Institute of Standards and Technology
Gaithersburg, MD, USA
ORCID: 0000-0002-1963-6039

Chris A. Michaels
National Institute of Standards and Technology
Gaithersburg, MD, USA
ORCID: 0000-0002-6562-4848

***Abstract*—Brillouin light scattering (BLS) offers an optical, noncontact, nondestructive method for probing the mechanical properties of next-generation semiconductor packaging materials. In this work, a switchable BLS microscope with both backscattered and off-axis configurations is presented. The microscope can be used for comprehensive modulus imaging, including longitudinal modulus, Young's modulus, shear modulus, bulk modulus, and Poisson's ratio. The capabilities of this microscope are demonstrated by measuring two proof-of-concept heterogeneous samples, including a polymer with two different degrees of cure (DoC) and a polymer with silica filler particles present. The modulus measurements performed by BLS are compared to results from conventional modulus measurement techniques, including nanoindentation (NI) and dynamic mechanical analysis (DMA). The BLS-derived modulus values are larger than those collected using NI and DMA due to differences in the frequency domain of the measurements, but are in agreement with literature trends. This microscope platform will be useful in evaluating mechanical heterogeneities in semiconductor packaging materials, to aid in the development of new packaging materials and standards, as well as providing insights to limit warpage issues in these materials.**

Keywords—Brillouin light scattering spectroscopy, microscopy, imaging, mechanical properties, packaging polymers

I. Introduction

As traditional semiconductor scaling is reaching its limits, continued performance gains increasingly rely on new advanced packaging paradigms such as 3D heterogenous integration (HI) [1, 2]. HI involves vertically stacking multiple components into a single footprint, and includes increasingly fine lines, pitch interconnects, as well as an increasing number of distribution layers. Advancements in packaging materials and metrology are needed to address these demanding constraints, as packaging governs both the mechanical integrity and the thermal/dielectric environment of the interconnect network [1, 3]. With increasing integration density, thermal and interfacial effects become tightly coupled, and variations in the local degree of cure (DoC) have a drastic effect on mechanical properties [4], moisture uptake [5], heat transfer [6], and dielectric response [7]. These variations are often heterogeneous at the micron scale, especially near interfaces and filler particles, and evolve with processing conditions such as cure time and temperature. Understanding and quantifying these spatially varying properties is essential for building predictive models of reliability and for informing design rules in advanced packaging [3]. Achieving this requires new metrology platforms capable of locally probing elastic moduli with both high sensitivity and spatial resolution.

Brillouin light scattering (BLS) spectroscopy has emerged as a powerful tool for this purpose [8]. BLS is an optical, noncontact, nondestructive technique, making it ideal for measuring mechanical property changes as a function of curing or upon post-cure temperature cycling. The technique probes the inelastic scattering of photons following interaction with acoustic phonons in the material. The frequency shift of the scattered light, which is usually in the range of 5 GHz to 20 GHz, can be used to calculate the elastic modulus. While both longitudinal and shear modes can be probed using BLS, to date, most BLS microscopes have been limited to measuring the longitudinal modulus using backscattered configurations [8, 9]. While useful, longitudinal measurements alone cannot fully describe the elastic behavior of the material. The ability to probe shear modes is critical, as it enables the determination of Young's modulus, shear modulus, bulk modulus, and Poisson's ratio. This comprehensive modulus dataset is indispensable for accurate predictive modeling of packaging reliability. However, the measurement of shear modes in polymers and polymer composites is technically challenging: shear BLS signals are typically only ≈ 1 % of the intensity of longitudinal BLS signals,

National Institute of Standards and Technology Award #70NANB24H111

have small BLS shifts that can be difficult to distinguish from the elastic peak, and cannot be measured in backscattered configurations [8, 9]. Instead, techniques such as off-axis microscopy or the preparation of samples in difficult-to-manufacture geometries such as platelets are needed [9, 10].

In this work, we present a switchable longitudinal-shear BLS microscope that enables comprehensive modulus imaging of semiconductor packaging materials within a single, versatile platform. This is a significant advancement over our previous work of developing a microscope in a backscattered geometry capable of only probing longitudinal modes [11]. This metrology innovation allows for rapid switching between backscattered (longitudinal) and off-axis (shear) configurations by designing the system to incorporate movable and removable fixtures that minimize downtime and the need for realignment. Additionally, an electron-multiplying charge-coupled device (EMCCD) detector is integrated into our custom-built BLS spectrometer, enabling the reliable measurement of relatively weak shear BLS signals. These advances allow for imaging of shear BLS spectra in polymer-based packaging materials.

Using this platform, comprehensive modulus imaging can be performed to measure spatial inhomogeneities in the elastic properties of packaging materials. This capability is especially important for identifying local variations in modulus associated with cure heterogeneity and filler dispersion, among other properties. Samples with different DoC and with filler particles are measured as a proof-of-concept demonstration. The extracted values of Young's modulus and shear modulus via BLS are cross-validated with traditional elastic property characterization techniques, including nanoindentation (NI) and dynamic mechanical analysis (DMA).

By developing a single-platform metrology solution for switchable longitudinal and shear BLS imaging, this work establishes a new benchmark for characterizing the elastic moduli of packaging materials. Beyond providing comprehensive elastic constants, the microscope enables future investigation in the research areas of *in situ* monitoring of cure evolution, post-cure degradation, and interface-specific mechanics, all of which are directly relevant to package warpage, reliability, and lifetime prediction.

II. Methods

A. Brillouin Light Scattering Spectroscopy

In BLS, the velocities of the acousitic waves ν_x are calculated using [9]:

$$\nu_x = \frac{\lambda}{2n\sin\left(\frac{\theta}{2}\right)} \nu_B \quad , \tag{1}$$

where λ is the excitation wavelength, n is the refractive index, θ is the angle between the incident and scattered beams, and ν_B is the experimentally-measured frequency shift of the scattered light. The acoustic wave velocities calculated using (1) can then be used to calculate the elastic properties of the material. These velocities are related to the components of the elasticity tensor c_{ij}, which relates the stress and strain tensors, by [12]:

$$c_{ij} = \rho \nu_x^2 \quad , \tag{2}$$

where ρ is the density of the material. For an isotropic material, the elasticity tensor C_{ij} is defined as:

$$C_{ij} = \begin{bmatrix} c_{11} & c_{12} & c_{12} & 0 & 0 & 0 \\ c_{12} & c_{11} & c_{12} & 0 & 0 & 0 \\ c_{12} & c_{12} & c_{11} & 0 & 0 & 0 \\ 0 & 0 & 0 & c_{44} & 0 & 0 \\ 0 & 0 & 0 & 0 & c_{44} & 0 \\ 0 & 0 & 0 & 0 & 0 & c_{44} \end{bmatrix}. \tag{3}$$

The components of the elasticity tensor are related to the moduli of the material via:

$$c_{11} = M = \frac{1 - \sigma}{(1 + \sigma)(1 - 2\sigma)} Y \quad , \tag{4}$$

$$c_{12} = \frac{\sigma}{(1 + \sigma)(1 - 2\sigma)} Y \quad , \tag{5}$$

$$c_{44} = G = \frac{1}{2}(c_{11} - c_{12}) = \frac{1}{2(1 + \sigma)} Y \quad , \tag{6}$$

where M is the longitudinal modulus, σ is the Poisson's ratio, Y is the Young's modulus, and G is the shear modulus. From the Young's modulus and Poisson's ratio, the bulk modulus K can be calculated using:

$$K = \frac{1}{3(1 - 2\sigma)} Y \quad . \tag{7}$$

When probing an isotropic material using a backscattered excitation configuration ($\theta = 180°$), only the longitudinal acoustic wave (ν_L) can be measured as the magnitude of the shear acoustic wave (ν_S) is ≈ 0. While there is some off-axis light present in the backscattered configuration, it is of minor importance when using relatively low NA objectives and results in negligible shear signal. An off-axis configuration allows for the measurement of both ν_L and ν_S. Schematic diagrams of each of these configurations are shown in Fig. 1. In the off-axis configuration, the longitudinal scattered wave is the same polarization as the incident excitation beam (s-polarization as shown in Fig. 1), while the shear scattered wave is offset by 90° (p-polarization). In this work, s-polarization is referred to as V (i.e., vertical to the scattering plane), while p-polarization is referred to as H (i.e., horizontal to the scattering plane). Thus, longitudinal and shear scattering in the off-axis configuration are referred to as VV and VH, respectively.

Using right angle scattering ($\theta = 90°$, the optimal scattering angle to maximize the shear signal), the ratio of the magnitudes of the longitudinal (I_L) and shear BLS signals (I_S) can be calculated from the differential scattering cross sections of the acoustic phonons, leading to [9, 12]:

$$\frac{I_S}{I_L} = \left(\frac{\nu_S}{\nu_L}\right)^2 \left(\frac{p_{44}}{p_{12}}\right)^2 \quad , \tag{8}$$

where p_{12} and p_{44} are the Pockels elasto-optic coefficients.

As $\left(\frac{\nu_S}{\nu_L}\right)^2$ is less than 1 and $\left(\frac{p_{44}}{p_{12}}\right)^2$ is ≈ 0.01 for solid materials with high mechanical strength [9], the shear signal intensity is

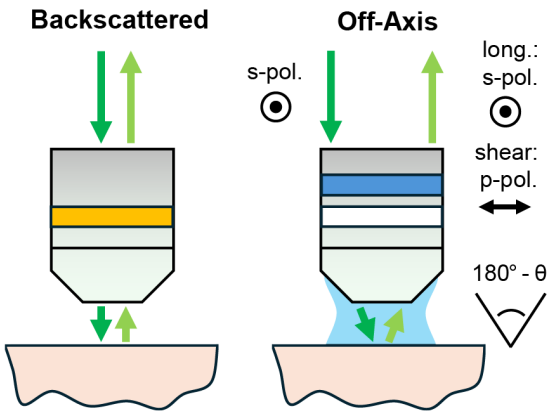

Fig. 1 Schematic diagram of backscattered and off-axis excitation. Backscattered measurements are performed in air, while off-axis measurements are performed in water. pol. and long. are used as shorthand for polarization and longitudinal, respectively.

much lower than the longitudinal signal. Furthermore, for scattering angles > 90° the intensity ratio is geometrically hindered. For these reasons, shear measurements typically require significantly longer exposure times, higher excitation powers, and/or high sensitivity detectors to enable reliable measurements.

B. Microscopy Platform

The microscope platform consists of a custom-designed confocal BLS microscope with a switchable backscattered and off-axis excitation configuration (Fig. 2). A 532 nm single longitudinal mode frequency-doubled Nd:YAG laser (Coherent VERDI V6) is used as the excitation source. The excitation light is coupled into a microscope enclosed by a blackout box using a single mode optical fiber (SMF). The beam is collimated and passes through a clean-up filter (OptiGrate BragGrate Bandpass Filter, bandwidth < 150 pm) and a half waveplate (HWP) to tune the polarization axis. A removable mirror allows for switching between the backscattered and off-axis paths.

Along the backscattered path, the beam passes through a beam expander to adjust the beam size to overfill the back aperture of the microscope objective. The beam then passes through a circulator, consisting of a polarizing beamsplitter (PBS), and a quarter waveplate (QWP), and is reflected off of a non-polarizing beamsplitter (BS) to be directed into the microscope objective (Olympus 20x, NA0.45). Backscattered light is primarily reflected off of the BS, with some light passing through to allow for imaging using a camera (Pixelink). The reflected light passes through the circulator and along the collection path.

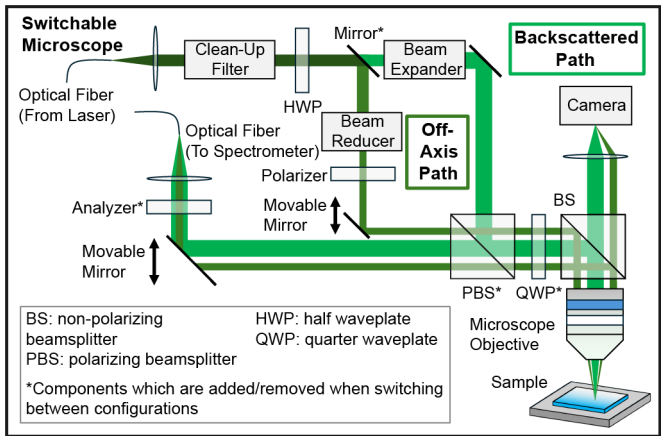

Fig. 2 Schematic diagram of the switchable BLS microscope.

The off-axis path requires a small excitation beam offset from the center of the microscope objective [9]. To this end, along this path, the beam size is adjusted using a beam reducer. The beam is linearly polarized (s-polarization) using a polarizer, and the position of a movable mirror is adjusted to allow for appropriate coupling into the microscope objective (Olympus 60x, NA1.20W). When switching between the backscattered and off-axis configurations, a movable mirror is adjusted to allow for coupling into a SMF directed into the spectrometer. In the case of the off-axis configuration, scattered light is collected from a solid angle centered at ≈ 130°. This angle is calculated using (1), by comparing the longitudinal frequency shifts in the backscattered and off-axis configurations [9]. Additionally, an analyzer is used to allow for selective probing of longitudinal (s-polarization) and shear (p-polarization) components in the off-axis configuration.

Details on elastic suppression and the spectrometer can be found in our previous publication [11]. Briefly, the light passes through an ultranarrow notch filter (LightMachinery Inc., "pump killer") to suppress the elastically-scattered light by ≈ 30 dB before being directed to the spectrometer. The spectrometer is a custom-built, two-stage virtually imaged phased array (VIPA)-based design inspired by the Scarcelli group [13, 14]. The VIPAs have free spectral ranges (FSRs) of 20 GHz and 30 GHz (LightMachinery Inc.). In order to allow for probing of the weak shear signals, the detector is changed to an EMCCD (Princeton Instruments ProEM 1024 eXcelon). The pixel location on the EMCCD is converted to a BLS shift using the nominal VIPA FSRs, focal lengths, and pixel dimensions with a dispersion model developed by Xu et al. [15]. A detector image of the elastically-scattered light is simulated and brought into agreement with the experimental image. The pixel-to-BLS shift is then extracted and used to unwrap the 2D detector image into a 1D BLS spectrum. The peaks are fit to Lorentzian line shapes to evaluate the spectral position.

For off-axis configuration measurements, the acquisition time varies from 1 s to 20 s and the electron multiplier gain is 100. In each configuration, the beam is generally focused to ≈ 20 µm below the surface to avoid excessive probe beam reflection and collection from the interface. The power incident on the sample is adjusted depending on the measurement, but is generally 10 mW to 40 mW. The microscope incorporates piezoelectric stages (Physik Instrumente) to move the sample and enable BLS imaging. For the longitudinal and shear imaging in the Comprehensive Modulus Imaging of Heterogeneous Polymers section, the image size is ≈ 170 µm x 170 µm, with a spacing of ≈ 10 µm and ≈ 20 µm, respectively. For the longitudinal and shear imaging in the Modulus Imaging of Polymers with Fillers section, the image size is ≈ 200 µm x 200 µm, with a spacing of ≈ 4 µm and ≈ 12 µm, respectively.

For the BLS data in the Modulus Cross-Validation section, the modulus values are calculated from 225 longitudinal and 100 shear data points. When generating images requiring both the VH and VV BLS shifts, i.e. the moduli, the VH array is resized using a bilinear spline. The VH BLS shift images and all of the dependent images (Young's modulus, shear modulus, and Poisson's ratio) are filtered using a median filter with a size of 3 pixels. The dependent images are filtered after calculation of the properties. For modulus calculations, the refractive index and material density are assumed to be homogenous and constant, which can lead to an underestimation of the property variations across the images.

C. Nanoindentation

Load-controlled NI is performed using a Nano Indenter XP system (MTS Nano Instruments). A sapphire spherical indenter with a nominal tip radius of 5 μm is used to minimize plastic deformation. The effective tip radius is measured to be 5.2 μm and 7.7 μm for indentations with depths of 20 nm to 50 nm and 100 nm to 200 nm, respectively, as estimated using previously published methods [16]. The loading, hold, and unloading times are 5 s, 0.2 s, and 5 s, respectively. The short segment times help to limit the effect of viscous deformation. The maximum load is 1 mN, and two 4 x 4 arrays of indentations with a spacing of 50 μm are performed to allow for averaging. A few outlier indentations, likely due to local surface roughness or other factors, are excluded from the analysis. The instrument software automatically accounts for thermal drift. The zero-point offsets for the load and displacement are taken into account using previously published methods, by fitting data from ≈ 5 % to 95 % of the maximum load [17]. Machine compliance is then accounted for by comparing the experimentally-measured displacement to the theoretical displacement for a Si sample, using a maximum load of 1 mN [16].

Due to the reasonably elastic behavior observed in the polymer sample, the loading curve (loading range: 15 % to 95 %) is fit to the elastic relationship for a spherical indenter based on Hertz theory [16, 17]:

$$P = \frac{4}{3} R^{\frac{1}{2}} E_R h^{\frac{3}{2}} , \tag{9}$$

where P is the indentation load, R is the tip radius, E_R is the reduced modulus, and h is the indenter displacement. E_R is defined as [16]:

$$\frac{1}{E_R} = \frac{1 - \sigma_i^2}{Y_i} + \frac{1 - \sigma_s^2}{Y_s} , \tag{10}$$

where σ_i and σ_s are the Poisson's ratios of the indenter and sample, respectively, and Y_i and Y_s are the Young's moduli of the indenter and sample, respectively. For a sapphire indenter, Y_i and σ_i are 403 GPa and 0.24, respectively. σ_s is estimated using BLS data to be ≈ 0.36.

D. Dynamic Mechanical Analysis

DMA is performed using an ARES-G2 rheometer (TA Instruments) with a rectangular torsion fixture and a liquid nitrogen filled forced convection oven for temperature control. All measurements are performed at (25.00 ± 0.05) °C. Amplitude sweeps are performed from 0.001 % to 0.1 % strain using a frequency of 1 Hz. A frequency sweep experiment is performed at 0.01 % strain from 10 Hz to 1 mHz. Three amplitude sweep and one frequency sweep experiments are performed.

E. Materials

The primary polymer used in this study is a bisphenol F diglycidyl ether/diethyl toluene diamine (DEGBF/DETDA)-based testing material under development as a research-grade test material (TM-1). To prepare the uncured epoxy resin, the DEGBF (Epon 862, Westlake Epoxy) and DETDA curing agent (Epikure W, Westlake Epoxy) are individually degassed using a planetary mixer (FlackTek, Inc., Speedmixer DAC 400.2 VAC-P) at a pressure of 10 kPa and a spinning rate of 42 Hz for 5 min. The degassed components are then combined at a stoichiometric ratio and are mixed following an identical procedure to the initial degassing. Resin samples are cured on a glass plate with an aluminum-backed fluorinated ethylene propylene (FEP) adhesive applied to the glass surface to assist in sample removal. To produce samples of well-defined thicknesses, resin is pipetted onto the FEP-coated glass plate, and covered with glass microscope slides with 0.1 mm thick glass microscope coverslips acting as spacers on either side of the resin. Free-standing films are prepared in the same manner, with the FEP also applied to the glass slide before covering the resin. For DMA testing, 1 mm thick glass slides are used as spacers. There are three curing schedules used for TM-1 in this work: Schedule A involves curing in a convection oven for 8 h at 120 °C. Schedule B uses a 80 °C cure for 1 h, followed by a 150 °C cure for 2.5 h. For both Schedule A and Schedule B the ramp rate is 5 °C/min. Cooling is performed passively to room temperature (RT) before removal from the oven. Schedule C involves curing at RT for several days.

To fabricate the heterogeneous polymer sample for the Comprehensive Modulus Imaging of Heterogeneous Polymers section, a side-by-side TM-1 sample with one side cured using Schedule B and one side cured using Schedule C is fabricated. The Schedule B side is cured using coverslip spacers as described above. Resin cured using Schedule C is then placed next to the Schedule B side and a piece of glass is placed on top of it. The resin is slowly pressed first by hand and then by using a C clamp to create a single sample with a uniform thickness. TM-1 samples fabricated using Schedule A are used in the Modulus Cross-Validation section. For NI, a free-standing film is mounted on an aluminum puck using superglue. For DMA, 13 mm x 55 mm x 1 mm rectangular bars are laser cut from the cured films. For BLS, a sample mounted on a glass coverslip is used.

To fabricate the epoxy/filler composite necessary for the Modulus Imaging of Polymers with Fillers section, a bisphenol A diglycidyl ether (DGEBA)-based two-component epoxy (Hardman 4004) is also tested using a 2:1 mass ratio of epoxy to curing agent. The Hardman 4004 resin and hardener are mixed for 2 min. Non-porous silica filler (Sigma Aldrich, average particle diameter of 50 μm) is then added to achieve a filler:epoxy mass ratio of 0.1:1. The mixture is then stirred for 3 min and drop-cast onto a polytetrafluoroethylene (PTFE) sheet for curing overnight at RT. Polycarbonate is used as a comparison of the capabilities of the backscattered and off-axis

configurations in the Microscope Configuration Comparison section.

In BLS calculations, the density of the TM-1 and Hardman samples is taken as 1.20 g/cm^3 and 1.10 g/cm^3, respectively, while the refractive indices are taken as 1.55 and 1.50, respectively.

III. Results & Discussion

A. Microscope Configuration Comparison

Polycarbonate spectra from each of the two configurations, normalized by the incident excitation power and exposure time, are shown in Fig. 3. The low magnitude of the shear signal demonstrates the need for an EMCCD as the detector. When using a conventional CCD or an sCMOS camera, shear measurements generally require multiple accumulations at the same location, leading to long acquisition times and potentially damaging to the sample, or averaging the signal from multiple locations, making high-resolution imaging impractical or impossible.

The off-axis configuration allows for collection of both longitudinal and shear data from the same spatial locations, enabling comprehensive modulus imaging. However, the backscattered configuration has several advantages over the off-axis configuration for longitudinal data collection. The off-axis configuration requires the use of a high NA objective to facilitate a scattering angle approaching 90°, making data collection using long working distance objectives challenging. This can be limiting for *in situ* monitoring of processes such as curing [11], which generally require the use of an environmental chamber. As shown in Fig. 3, the magnitude of the normalized longitudinal signal is higher in the backscattered configuration by a factor of ≈ 10 for this microscope platform. Additionally, the backscattered configuration enables a smaller spot size, facilitating high spatial resolution imaging. Lastly, the calculation of longitudinal modulus is simplified in the case of the backscattered configuration, as the scattering angle is known and does not require additional measurements to be calculated.

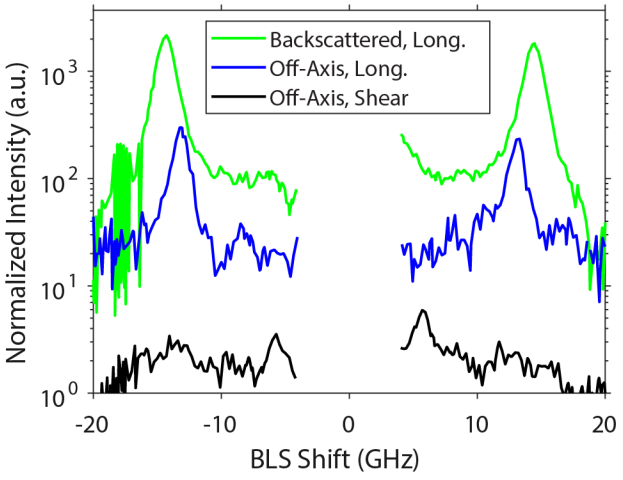

Fig. 3 Brillouin light scattering (BLS) spectra of polycarbonate using the two configurations. In the off-axis configuration, both longitudinal and shear spectra are shown. The spectra are normalized by the acquisition time and the excitation power incident on the sample.

Each of the two configurations has utility and offers trade-offs depending on the measurement needs. Results from the backscattered configuration can be found in our previous publication [11]; therefore, the remaining sections of this paper focus on data collected using the off-axis configuration.

B. Comprehensive Modulus Imaging of Heterogeneous Polymers

In order to evaluate the ability of the microscope to measure heterogeneous polymers, a proof-of-concept sample with intentional heterogeneity is tested, as shown in Fig. 4. The sample has two regions with different DoC (Fig. 4a) due to the two cure schedules used in fabricating the sample. The region which underwent Schedule B is more fully cured than the Schedule C region, and has larger BLS shifts in both VV (longitudinal, Fig. 4b) and VH (shear, Fig. 4c) polarizations. The BLS shifts are relatively consistent within each region, with a clear boundary separating the two regions. Using (4), (5), (6), and (7), as well as the density and refractive index, it is possible to perform a comprehensive modulus analysis and generate modulus images. The Young's modulus, shear modulus, and Poisson's ratio are shown in Fig. 4d-f, respectively. Each mechanical property has a relatively consistent value within each region, while at the same time it is possible to resolve clear differences between the two regions. The Schedule B region has higher Young's modulus and shear modulus values than the Schedule C region, which is in line with the Schedule B region being more fully cured and therefore brittle, as opposed to the rubbery Schedule C region. There are several missing points in the BLS shift, VH image, which propagate to the calculated properties in the other images. This poor fitting is likely due to defects in the sample such as poor wetting to the glass coverslip or noise in the relatively weak shear data. Images of the longitudinal modulus and bulk modulus can also be generated using (4) and (7), respectively, but are omitted from Fig. 4 for brevity.

C. Modulus Imaging of Polymers with Fillers

Further proof-of-concept measurements are performed on a sample fabricated with inorganic filler particles. As shown in Fig. 5, the microscope can be used to perform comprehensive modulus evaluations of the polymer in between the silica filler particles. There is some scatter present in the modulus values and a slight trend of increasing modulus from the bottom to the top of the images, possibly indicating heterogeneity due to poor mixing or measurement error due to thermal or laser wavelength drift. In Fig. 5, there are no prominent trends observed in either the Young's modulus or shear modulus in the vicinity of the particles compared to farther from the particles. While nanomechanical characterization of polymer-silica interfaces by atomic force microscopy (AFM) and fluorescence spectroscopy have revealed interphase regions with different mechanical properties within ≈ 10 nm to 200 nm of the polymer-silica interface [18, 19, 20], probing variations in mechanical properties on this length scale is difficult to

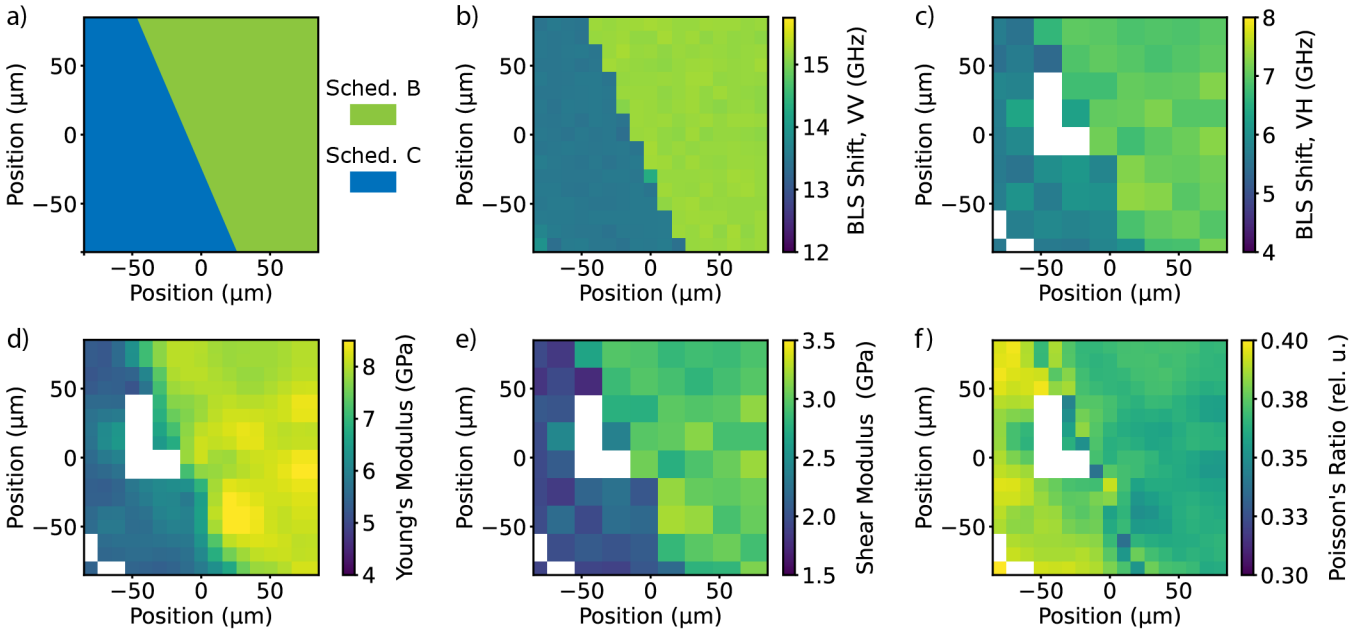

Fig. 4 Comprehensive modulus imaging of TM-1 with two different cure schedules (see Materials section for details). (a) Schematic, (b) BLS shift, VV polarization, (c) BLS shift, VH polarization, (d) Young's modulus, (e) shear modulus, and (f) Poisson's ratio. In the images, white regions indicate missing data due to poor peak fitting.

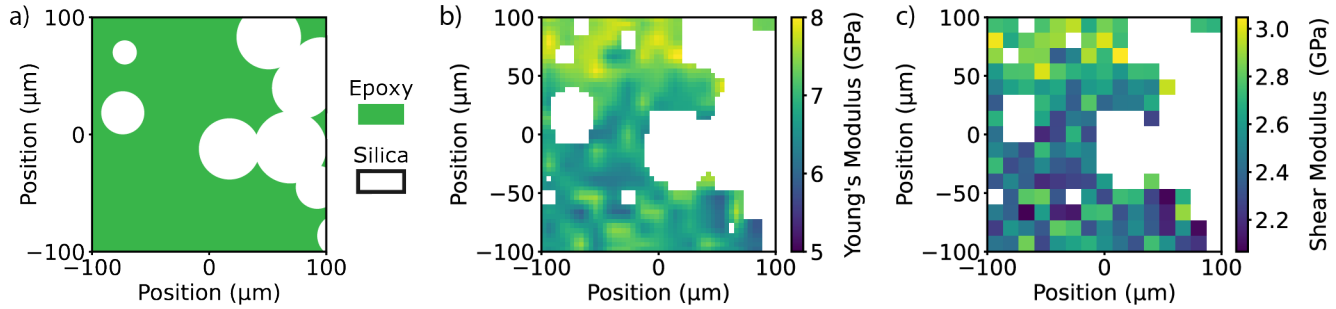

Fig. 5 Modulus imaging of a sample with embedded fillers (see Materials section for details). (a) Schematic, (b) Young's modulus, and (c) shear modulus. In the modulus images, white regions indicate missing data, either because of a lack of data in the silica filler regions or poor peak fitting.

impossible using optical techniques such as BLS. In the backscattered configuration the BLS spot size is diffraction limited but comparably large due to the low numerical aperture (NA) of the microscope objective, which is necessary to limit broadening of the BLS peak [8]. In the off-axis configuration, the spot size is enlarged due to the oblique incident angle. Furthermore, BLS probes the mechanical properties via interaction with the phonon modes within the material, which in epoxies have wavelengths on the order of hundreds of nanometers. However, BLS microscopy is highly useful for process verification, enabling the assessment of DoC or poor mixing in the general vicinity of particles and joints.

When focusing within the silica particles, the signal is not strong enough to meaningfully probe any mechanical properties using this microscope due to the weak scattering cross section of glass materials [9]. For this reason, any lack of signal due to voids arising from poor wetting of the epoxy to the silica particles is difficult to probe. This microscope is still under development, and it will be modified to enable both measurement of silica filler particles and higher resolution imaging, making it better suited for evaluating state-of-the-art underfills with smaller filler particle sizes.

D. Modulus Cross-Validation

To validate the modulus values analyzed using the BLS microscope, BLS moduli results are compared to conventional measurements performed by NI and DMA. In each of the experiments, TM-1 is cured using Schedule A for comparability. Representative fitted curves for the BLS and NI results as well as amplitude- and frequency-dependent DMA results are shown in Fig. 6. The storage modulus shown in Fig. 6a is the real part of the shear modulus. The modulus results for each of the techniques are tabulated in Table I.

The Young's modulus value of (3.2 ± 0.2) GPa analyzed from NI is comparable to experimental results in literature for DEGBF/DETDA-based materials collected using NI (3.61 GPa, [21]) and using other techniques (2.72 GPa, [21], and 2.56 GPa, [22]). Reported molecular dynamics simulations (MD) Young's modulus values are also similar to the experimental NI results (2.0 GPa to 3.5 GPa, [23]), with the reported mechanical response being strongly dependent on the degree of crosslinking

and the MD method used. As shown in Fig. 6a, the shear modulus value collected via DMA is 1.1 GPa to 1.2 GPa, with

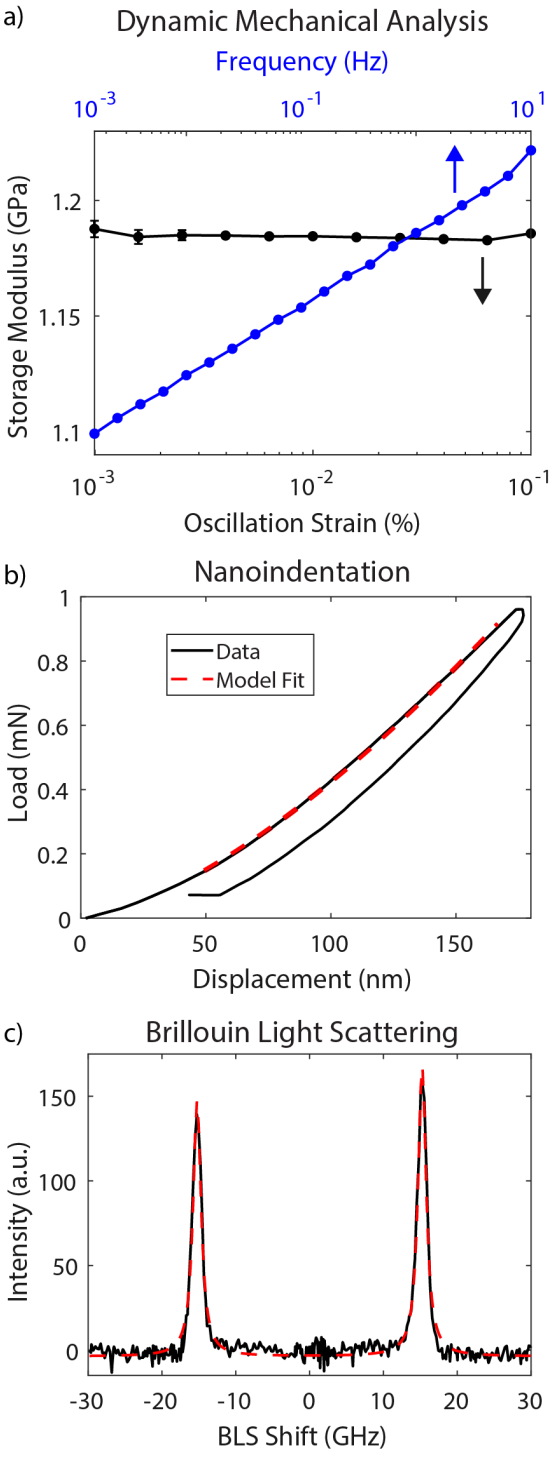

Fig. 6 Characterization of TM-1 using various techniques for modulus comparison study. (a) Dynamic mechanical analysis results. Note that the storage modulus is the real component of the shear modulus. The points and error bars in the strain-dependent measurements represent the mean and standard deviation, respectively, from three measurements. Representative (b) nanoindentation and (c) longitudinal Brillouin light scattering (BLS) results. The BLS spectrum is an average over 225 points.

TABLE I. COMPARISON OF ELASTIC MODULI MEASURED USING DIFFERENT TECHNIQUES.

	Nano-indentation	**Dynamic Mechanical Analysis**	**Brillouin Light Scattering**
Frequency Range	Quasi-static	1 mHz - 10 Hz	≈ 5 GHz - 20 GHz
Young's Modulus (GPa)	3.2 ± 0.2[a]		8.3 ± 1.1[b]
Shear Modulus (GPa)		1.1 - 1.2	3.1 ± 0.2[b]

[a] The ± is indicative of the standard deviation due to random uncertainties involved in the measurement.

[b] The ± is indicative of both the random and systematic uncertainties involved in the measurements.

the modulus increasing slightly with respect to increasing frequency. These values compare favorably to experimental and MD literature results for shear modulus (0.95 GPa, [22], and 0.7 GPa to 1.3 GPa, [23]).

In the case of both the Young's and shear moduli, the experimentally-measured BLS values are higher than the NI and DMA values by a factor of ≈ 2.75, as shown in Table I. This is likely due to the difference in frequency domain for each of these measurements, as NI and DMA are performed at quasi-static conditions or relatively low frequencies, while BLS measures the elastic response in the GHz range. This has a strong impact on the measured elastic response, with higher response frequencies often resulting in larger modulus values, as reported for both epoxies [24] and other soft materials [25, 26]. This phenomenon has been attributed to a decrease in polymer chain mobility at high frequencies [24] or a lack of material relaxation because of the high rate of stress [25, 26]. However, to our knowledge, measurements across a large frequency range on semiconductor packaging materials is lacking; therefore, further mechanistic investigation is needed to link BLS-derived modulus values to quasi-static and other low-frequency modulus measurements.

Using (4), (5), and (6), the Poisson's ratio of the TM-1 material is calculated as ≈ 0.36. This compares favorably to measurements of DEGBF/DETDA-based materials in literature performed at comparatively low frequencies, with values of 0.35 to 0.43 being reported [21, 23].

IV. CONCLUSIONS

A switchable BLS microscope is presented with two configurations: 1) a backscattered mode for fast, high-resolution longitudinal measurements, and 2) an off-axis mode for both longitudinal and shear measurements. The microscope is used to perform comprehensive elastic modulus measurements on two proof-of-concept heterogeneous samples with relevance for semiconductor packaging materials: 1) a material with two different DoC, and 2) a material with embedded filler particles. Clear differences are apparent between the sample with two different DoC, and measurements of the epoxy between silica filler particles is demonstrated. The moduli collected using the switchable BLS microscope are compared to both experimentally-collected NI and DMA results, as well as other mechanical characterization performed in literature. While some differences exist in the modulus values in this comparison, this

is likely due to differences in the frequency domain of the measurements.

The capabilities of this switchable BLS microscope are important when evaluating the mechanical properties of semiconductor packaging materials with nonuniform DoC and around interfaces. The insights provided by this single-platform metrology solution will be instrumental in the effort to develop new packaging standards, as well as to address warpage issues. Future work involves improving the microscope platform to enable higher resolution imaging and measurement of silica filler particles to differentiate particles from voids and other defects in the material, as well as correlating BLS measurements to those measurements performed at quasi-static and low-frequency conditions.

Acknowledgment

This work was performed with funding from the CHIPS Metrology Program, part of CHIPS for America, National Institute of Standards and Technology, U.S. Department of Commerce. This work was performed under financial assistance award 70NANB24H111 from the National Institute of Standards and Technology, U.S. Department of Commerce.

Data Availability

All data associated with this paper are publicly available through the NIST Public Data Repository at https://doi.org/10.18434/mds2-4059 [27].

Disclaimer

Certain commercial equipment, instruments, software, or materials are identified in this paper in order to specify the experimental procedure adequately. Such identification is not intended to imply recommendation or endorsement by NIST, nor is it intended to imply that the materials or equipment identified are necessarily the best available for the purpose. The statements, findings, conclusions, and recommendations are those of the author(s) and do not necessarily reflect the views of the National Institute of Standards and Technology or the U.S. Department of Commerce.

References

[1] Z. Chen, J. Zhang, S. Wang, and C.-P. Wong, "Challenges and prospects for advanced packaging," *Fundam. Res.*, vol. 4, no. 6, pp. 1455–1458, Nov. 2024.

[2] "Heterogeneous integration roadmap." [Online]. Available: https://eps.ieee.org/hir

[3] R. Tao *et al.*, "Material needs and measurement challenges for advanced semiconductor packaging: understanding the soft side of science," *IEEE Trans. Compon. Packag. Manuf. Technol.*, vol. 15, no. 10, pp. 2071–2082, Oct. 2025.

[4] S. P. Phansalkar, C. Kim, and B. Han, "Effect of critical properties of epoxy molding compound on warpage prediction: A critical review," *Microelectron. Reliab.*, vol. 130, p. 114480, Mar. 2022.

[5] J. B. Enns and J. K. Gillham, "Effect of the extent of cure on the modulus, glass transition, water absorption, and density of an amine-cured epoxy," *J. Appl. Polym. Sci.*, vol. 28, no. 9, pp. 2831–2846, Sep. 1983.

[6] G. Struzziero, B. Remy, and A. A. Skordos, "Measurement of thermal conductivity of epoxy resins during cure," *J. Appl. Polym. Sci.*, vol. 136, no. 5, p. 47015, Feb. 2019.

[7] Y. Yang *et al.*, "Fully integrated flexible dielectric monitoring sensor system for real-time *in situ* prediction of the degree of cure and glass transition temperature of an epoxy resin," *IEEE Trans. Instrum. Meas.*, vol. 70, pp. 1–9, Feb. 2021.

[8] I. Kabakova *et al.*, "Brillouin microscopy," *Nat. Rev. Methods Primer*, vol. 4, no. 1, p. 8, Feb. 2024.

[9] M. Kim *et al.*, "Shear Brillouin light scattering microscope," *Opt. Express*, vol. 24, no. 1, pp. 319–328, Jan. 2016.

[10] M. Guerette and L. Huang, "A simple and convenient set-up for high-temperature Brillouin light scattering," *J. Phys. Appl. Phys.*, vol. 45, no. 27, p. 275302, Jun. 2012.

[11] S. Engmann, A. J. Gayle, S. K. Romberg, C. L. Soles, and C. A. Michaels, "A dual mode Brillouin/low-frequency Raman spectroscopy microscope for local mechanical property imaging for semiconductor packaging materials," in *2025 IEEE 75th Electronic Components and Technology Conference (ECTC)*, Dallas, TX, May 2025, pp. 1694–1701.

[12] K. Elsayad *et al.*, "Mechanical properties of cellulose fibers measured by Brillouin spectroscopy," *Cellulose*, vol. 27, pp. 4209–4220, May 2020.

[13] K. Berghaus, J. Zhang, S. H. Yun, and G. Scarcelli, "High-finesse sub-GHz-resolution spectrometer employing VIPA etalons of different dispersion," *Opt. Lett.*, vol. 40, no. 19, pp. 4436–4439, Sep. 2015.

[14] G. Scarcelli and S. H. Yun, "Multistage VIPA etalons for high-extinction parallel Brillouin spectroscopy," *Opt. Express*, vol. 19, no. 11, pp. 10913–10922, May 2011.

[15] J. Xu, M. Liu, N. Luo, Z. Hao, X. He, and J. Shi, "Orthogonal dispersion modeling of double-stage VIPA spectrometer in SBS system," *Opt. Express*, vol. 32, no. 23, pp. 41524–41538, Nov. 2024.

[16] T. Chudoba, N. Schwarzer, and F. Richter, "Determination of elastic properties of thin films by indentation measurements with a spherical indenter," *Surf. Coat. Technol.*, vol. 127, no. 1, pp. 9–17, May 2000.

[17] S. Pathak, J. Shaffer, and S. R. Kalidindi, "Determination of an effective zero-point and extraction of indentation stress–strain curves without the continuous stiffness measurement signal," *Scr. Mater.*, vol. 60, no. 6, pp. 439–442, Mar. 2009.

[18] M. Zhang, S. Askar, J. M. Torkelson, and L. C. Brinson, "Stiffness gradients in glassy polymer model nanocomposites: comparisons of quantitative characterization by fluorescence spectroscopy and atomic force microscopy," *Macromolecules*, vol. 50, no. 14, pp. 5447–5458, Jul. 2017.

[19] I. Saito, R. J. Sheridan, S. Zauscher, and L. C. Brinson, "Pushing AFM to the boundaries: interphase mechanical property measurements near a rigid body," *Macromolecules*, vol. 58, no. 2, pp. 980–988, Jan. 2025.

[20] D. W. Collinson, R. J. Sheridan, M. J. Palmeri, and L. C. Brinson, "Best practices and recommendations for accurate nanomechanical characterization of heterogeneous polymer systems with atomic force microscopy," *Prog. Polym. Sci.*, vol. 119, p. 101420, Aug. 2021.

[21] D. R. Klimek-McDonald, J. A. King, I. Miskioglu, E. J. Pineda, and G. M. Odegard, "Determination and modeling of mechanical properties for graphene nanoplatelet/epoxy composites," *Polym. Compos.*, vol. 39, no. 6, pp. 1845–1851, Jun. 2018.

[22] J. L. Tack, "Thermodynamic and mechanical properties of Epon 862 with curing agent DETDA by molecular simulation," Texas A&M University, 2006.

[23] S. V. Kallivokas, A. P. Sgouros, and D. N. Theodorou, "Molecular dynamics simulations of EPON-862/DETDA epoxy networks: structure, topology, elastic constants, and local dynamics," *Soft Matter*, vol. 15, pp. 721–733, Jan. 2019.

[24] J. Feng and Z. Guo, "Effects of temperature and frequency on dynamic mechanical properties of glass/epoxy composites," *J. Mater. Sci.*, vol. 51, pp. 2747–2758, Mar. 2016.

[25] R. Rodríguez-López *et al.*, "Network viscoelasticity from Brillouin spectroscopy," *Biomacromolecules*, vol. 25, no. 2, pp. 955–963, Feb. 2024.

[26] A. D. Mulliken and M. C. Boyce, "Mechanics of the rate-dependent elastic–plastic deformation of glassy polymers from low to high strain rates," *Int. J. Solids Struct.*, vol. 43, no. 5, pp. 1331–1356, Mar. 2006.

[27] A. J. Gayle *et al.*, "Data for a switchable longitudinal & shear BLS microscope for comprehensive modulus imaging of semiconductor packaging materials," *Natl. Inst. Stand. Technol.*, 2026, doi: 10.18434/mds2-4059.